Embedded Distributed Temperature Sensing Enabled Multi-State Joint Observation of Smart Lithium-Ion Battery

Zhongbao Wei, *Senior Member, IEEE*, Jian Hu, Hongwen He, *Senior Member, IEEE*, Yifei Yu, *Member, IEEE*, James Marco, *Member, IEEE*

***Abstract*—Accurate monitoring of the internal statuses are highly valuable for the management of lithium-ion battery (LIB). This paper proposes a thermal model-based method for multi-state joint observation, enabled by a novel smart battery design with embedded and distributed temperature sensor. In particular, a novel smart battery is designed by implanting the distributed fiber optical sensor (DFOS) internally and externally. This promises a real-time distributed measurement of LIB internal and surface temperature with a high space resolution. Following this endeavor, a low-order joint observer is proposed to co-estimate the thermal parameters, heat generation rate, state of charge, and maximum capacity. Experimental results disclose that the smart battery has space-resolved self-monitoring capability with high reproducibility. With the new sensing data, the heat generation rate, state of charge, and maximum capacity of LIB can be observed precisely in real time. The proposed method validates to outperform the commonly-used electrical model-based method regarding the accuracy and the robustness to battery aging.**

***Keywords*— Embedded sensor, distributed temperature measurement, smart battery, optical fiber sensor, heat generation rate.**

I. Introduction

Lithium-ion batteries (LIBs) are widely used for renewable energy storage and electrified transportation due to the high gravimetric/volumetric densities. Associated with the fast growth and foreseeable rising trend, the LIB management has been extensively studied over years [1-3]. Amongst others, the high-fidelity monitoring of internal statues of LIB underlies the implementation of other management algorithms.

Thermal states like the internal temperature and heat generation rate are critical to the thermal management and fault diagnostic of LIB. A variety of estimation methods have been discussed for LIB in recent review works [4]. The experimental approaches intend to measure the heat generation rate directly via approaches like accelerating rate calorimetry and isothermal heat conduction calorimetry [5, 6]. In spite of the accurate characterization, experimental protocols depend on expensive instruments and well-controlled environment, which are hardly met in practical *in-situ* applications.

Modeling methods calculate the heat generation rate based on the available measurements of LIB current, voltage. The heat generation models cover the electrochemical-thermal [7, 8] and the electrical-thermal types [9, 10], both of which have been applied to capture the thermal dynamics of LIB. An electrochemical-thermal model for a pouch LIB was proposed in [7] to calculate the heat generation considering the effects of C-rates and temperature. A three-dimensional electrochemical-thermal coupled model is developed in [8] to analyze the fault feature for internal short circuit detection. However, the computational burden for an electrochemical-thermal model composed by partial differential equations is too high to be applicable in practice. In contrast, electro-thermal models are more suitable for on-board applications. The thermal dynamics of LIB was analyzed in [11], where a lumped electro-thermal model is identified to calculate the battery temperature variation. By regarding a cylindrical LIB as an assembly of small cell sandwiches, a three-dimensional mesoscale thermal model was built in [10], where each of the cell sandwiches is modeled as an individual heat generation source.

In the aforementioned works, the heat generation rate was calculated with a heat generation model, and the temperature was calculated via a heat transfer model. In contrast, the heat generation rate was online estimated using dual-temperature measurements based on an inversed two-state heat transfer model in [12]. However, the modeling accuracy and online tractability can be hardly compromised to meet the requirement of practical application. Moreover, the determination of model parameters like the entropy coefficient is challenging [13]. Alternatively, the heat generation rate can be estimated directly by heat transfer analysis with alleviated computational effort, provided that the internal temperature of LIB and its dependent thermal parameters are known accurately. However, this is not necessarily in accordance with reality considering the limited access into the inner of commercial LIB configurations.

Manuscript received October 12, 2021; revised January 5, 2022, accepted January 21, 2022. This work was supported by the National Natural Science Foundation of China under Grant 52072038 (Corresponding author: Yifei Yu).

Z. Wei, J. Hu and H. He are with the National Engineering Laboratory for Electric Vehicles, School of Mechanical Engineering, Beijing Institute of Technology, China (e-mail: weizb@bit.edu.cn; 3120190329@bit.edu.cn; hwhebit@bit.edu.cn).

Y. Yu and J. Marco are with the Energy Innovation Centre, Warwick Manufacturing Group, University of Warwick, Coventry, United Kingdom (yifei.yu.1@warwick.ac.uk; James.Marco@warwick.ac.uk).

This barrier calls for an emergent need of *in-operando* LIB internal temperature sensing. This endeavor also benefits other management duties like the thermal fault diagnostic [14], thermal runaway pre-warning [15], and the thermal-conscious fast charging [16], etc.

Model-based observation is promising for the estimation of LIB internal temperature. The internal temperature and other states can be observed in a model-based filtering framework, provided that the electro-thermal [17, 18] or electrochemical-thermal models [19, 20] are available. In particular, the heat dynamics are modeled frequently by the lumped thermal network model [21, 22], before the temperature estimation is adopted. Illustratively, a sliding mode observer is designed to estimate the core temperature and SOC hierarchically in [18] using the measured current, voltage, and surface temperature. Although highly compatible to commercial LIB systems, the uncertainties rooted in disturbances, model mismatch, and remarkable computing cost can compromise their performance in real-time application.

Impedance-based methods have also been explored for LIB internal temperature estimation. Leveraging the temperature-dependent spectral responses, the battery temperature can be reversed easily from the measured impedances [23]. The impedance measurement is also easily extended. Illustratively, Kalman filter was used to estimate the core temperature with impedance measurement in [24]. The LIB core temperature was estimated combining the impedance and surface temperature in [25]. Impedance-based methods are computationally efficient and non-destructive. However, they need costly equipment or special circuit design to generate the exciting signals. Moreover, the spatial information is unclear as the measurement reflects a cumulative effect. The disturbance from state of charge (SOC) and state of health (SOH) to the spectral behavior are also difficult to be discriminated.

Such challenges solicit emerging interests to implant sensors inside the LIB for temperature sensing. Thermocouples were inserted inside LIB for temperature monitoring, but the large sensor size induces the risk of composite leakage at the sealing position [26]. Compared to wire-based sensors, the thin-film sensors can be embedded into the LIB more compactly [12, 27, 28]. Illustratively, a nickel foil is embedded into a cell for heating and temperature sensing in [12, 29]. However, the thin-film sensors can cover the active site of electrode and cause non-ignorable capacity losses. Concerning the dimension and mechanical strength, their compatibility with winding cells is also questionable.

Most recently, optical Fiber Bragg Grating (FBG) sensors have been reported for LIB monitoring, enjoying the benefits of quick response, high sensitivity, and multiplexed configuration [30]. An optical FBG sensor was inserted between the spacer and current collector of the cathode, and a temperature gradient of ~10 °C was found between inside and the ambient [31]. Novais et al. [32] embedded the optical FBG sensor between two separators to measure the LIB internal temperature of a coin cell. Authors from the same group [33-35] devised the optical FBG sensor into the core void of an 18650 cell. It was found the core temperature was 5 ℃ higher than the surface at 1 C discharge. Huang et al. [36] intruded a specially-designed single-mode optical fiber sensor into the jelly roll of a 18650 cell for internal temperature and pressure decoding. A mechanical structure-modified FBG sensor was designed in [37] to monitor the electrode temperature of a 60 Ahr LIB with a validated high sensitivity. However, pronounced temperature inhomogeneities exist inside the cells, especially for the fast-emerging large-format cells. In this regard, existing FBG sensing techniques lack sufficient space resolution for the local overheat or thermal fault detection. Moreover, the impact of FBG sensor embedment to the battery performance has not been sufficiently evaluated.

To date, embedded temperature sensing is still at a nascent stage requiring more exploration. Space-resolved, degradation-free, and *in-operando* internal temperature sensing will enable probing the thermal evolution and interface of LIB in practical utilizations. Moreover, the acquisition of distributive internal sensing data foreseeably extends the performance limitation of present battery management system. However, this has not been sufficiently studied before.

This paper aims to bridge aforementioned gaps and proposes a low-order multi-state joint observer enabled by a novel smart battery configuration with embedded distributed temperature sensing. The primary contributions are summarized as follows:

(1) A novel smart battery configuration is proposed, for the first time, by implanting the distributed optical fiber sensor (DFOS) internally and externally to the cylindrical cell. This innovation promises a real-time distributed sensing of the temperature matrix over both the core and surface of LIB, with a high space resolution of 2.6 mm.

(2) With the newly-obtained core temperature, a thermal model-based low-order joint observer, entirely different from the reported electrical model-based ones, is proposed to monitor the heat generation rate, SOC, and maximum capacity of battery simultaneously in a real-time fashion.

(3) The proposed joint observer depends on material-relevant thermal parameters which are stable over certain life span of LIB, instead of the commonly-used environmental-sensitive electrical parameters. This remarkably mitigates the need of frequent algorithm re-calibration.

This work is the first one we are aware of that develops the embedded DFOS-based cylindrical smart battery. Moreover, the associated low-order multi-state estimation enabled by embedded sensing has also never been disclosed before.

The remainder of this paper is organized as follows. The DFOS embedment and smart battery design are presented in Section II. Section III formulates the thermal model-based multi-state joint observer. Results are discussed in Section IV, while the major conclusions are drawn in Section V.

II. Embedded Distributed Temperature Sensing

A. Sensor Integration

A smart battery implanting DFOS is designed to realize the space-resolved measurement of LIB internal and surface

temperature in real time. Before the integration, the computerized tomography (CT) scanning and cell disassembling are performed to understand the cell internal structure. The detailed procedures of sensor embedment and smart battery integration are elaborate as follows.

First, the cell is fixed to a holder and a 0.9 mm hole is drilled into the center of negative terminal using the drilling machine, as shown Fig. 1 (a). The 0.9 mm hole in the negative terminal is sealed with Kapton tap to protect the internals of the cell. Second, the positive terminal is opened with a pipe cutter as illustrated in Fig. 1 (b). Specifically, the positive terminal needs to be isolated using the Kapton tape to prevent the occurrence of short circuit. Third, the DFOS is inserted from the negative terminal through the isolation layer, as shown in Fig. 1 (c, d). The DFOS is routed and mounted externally near to the positive current tab (D2) and negative current tab (D3) using Kapton tape, as shown in Fig. 1 (g). At this stage, the positive terminal needs to be resealed using adhesives and protected using Kapton tape after the adhesive is allowed to dry.

After the DFOS embedment and re-sealing, the instrumented smart cell is placed in the test rig and connected to a battery testing system via copper bus bars as shown in Fig. 1 (f). An overall illustration of the smart cell is shown in Fig. 1 (g), where D1 measures the internal temperature from the bottom (0 mm) to the top (63 mm) of the jellyroll with length of 63 mm. Meanwhile, D2 and D3 measure the external temperature near the positive tab and negative tab respectively with the same length of 63 mm.

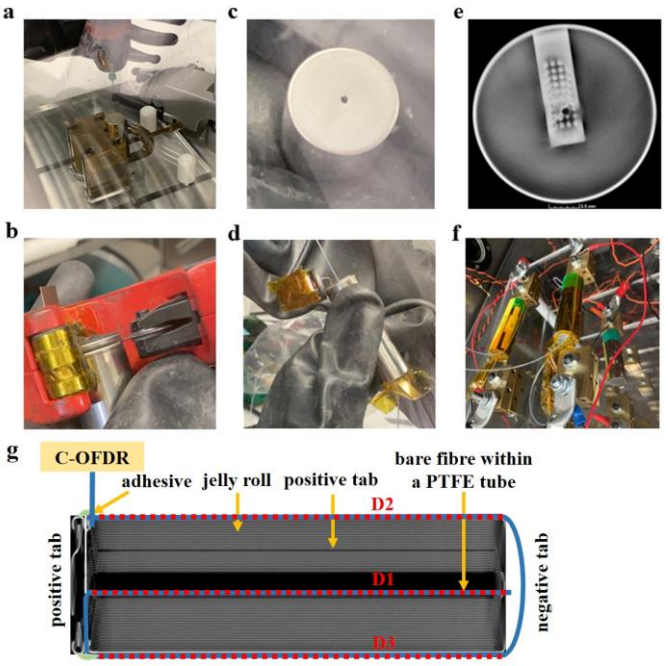

Fig. 1. Smart cell instrumentation process. a) hole drilling from negative terminal; b) positive terminal opening; c) hole drilled from the negative terminal; d) DFOS embedment and re-sealing; e) negative tab view of CT scanning after instrumentation; f) gluing the DFOS externally and connecting the cell into test rig; g) smart cell with DFOS for real-time internal (D1) and external (D2 and D3) temperature monitoring.

B. Rayleigh Scattering-Based DFOS

The DFOS for distributive temperature measurement is based on Rayleigh scattering. When an electromagnetic wave is launched into an optical fiber, the light is redistributed by Rayleigh scattering [31], [32]. If the local temperature change is relayed to the optical fiber, the scattered signal in the fiber is modulated. More details about this can be found in [33], [34]. The desired features of Rayleigh scattering-based fiber sensing allow distributed measurements with millimeter-scale spatial resolution and high measurement accuracy, making it a suitable solution for LIB *operando* and *in-situ* applications. In particular, Coherent Optical Frequency Domain Reflectometry (C-OFDR) is performed to monitor the distributed temperature. C-OFDR was selected for the high spatial resolution (approx. 2.6 mm).

Referring to the interference signal from the major interferometer, the beat frequency (f_B) is found to be mapped to a certain location (l) along the fiber. To this end, the generated spatial resolution is expressed by:

$$\Delta l = c/2n_g\Delta F \tag{1}$$

where n_g is the group refractive index, c is the light speed, ΔF is the frequency tuning range.

A unique *fingerprint* Rayleigh backscattered spectrum (RBS) can be obtained under a given working condition. The local RBS shifts in frequency once the environmental conditions like temperature and strain change. The cross-correlation between the fingerprint and the measured RBS defines the local spectral shift ($\Delta\nu$), which can be used to calculate the temperature along the whole fiber [36]. In particular, the changes in the local time-period of Rayleigh scattering causes spectral and temporal shifts in the locally-reflected spectrum, which can be calibrated to support the distributed sensing.

The shift in the spectrum of light scattered in the *DFOS* in response to strain and temperature is analogous to a shift in the spectral shift, $\Delta\nu_{DFOS}$**:**

$$\frac{-\Delta\nu_{DFOS}}{\nu} = K_T\Delta T_{measured} + K_\varepsilon\varepsilon_{measured} \tag{2}$$

where ν is the mean optical frequency, K_T and K_ε are the calibration coefficients regarding the temperature and strain, $\Delta T_{measured}$ and $\varepsilon_{measured}$ are the measured temperature change and strain.

This thermal effect is the coupling of the fiber thermal expansion and the temperature dependence of refractive index. Excluding the effect of strain, the frequency shift ($\Delta\nu_{T\text{-}DFOS}$) caused by the temperature variation is given by:

$$\frac{-\Delta\nu_{T-DFOS}}{\nu} = K_T\Delta T_{measured} \tag{3}$$

The coefficients are defined as common values for the germanosilicate core fibers, i.e., $K_T = 6.45 \times 10^{-6}$ °C^{-1} [31], [37]. Hence, ruling out the strain effect, the temperature change can be determined by:

$$\Delta T_{measured} = -\frac{1}{K_T\nu}\Delta\nu_{T-DFOS} = C_T\Delta\nu_{T-DFOS} \tag{4}$$

Assuming a scan center wavelength of 1550 nm [31], [37], the coefficients can be substituted in to yield the following temperature conversion factors:

$$C_T = -0.801°C/GH_z \tag{5}$$

To sum up, by measuring the frequency shift along the fiber and multiplying the temperature coefficient, the distributed temperature along the whole fiber can be obtained. It is worth noting that the DFOS is placed within a PTFE tube to fully eliminate the interference of strain effect, so that the resultant measurement is solely relevant to the temperature change. The diameter of the optical fiber is 125 μm and the diameter of the PTFE tube is 500 μm.

C. Impact to Battery Life Performance

In spite of the unique advantage of distributed internal temperature monitoring, it is imperative to evaluate the impact of DFOS embedment to the battery performance. To this end, characterization and repeatability tests are carried out on the modified smart cell and the original cell. The comparative results shown in Fig. 2 are critical to highlight that the DFOSs do not adversely affect the cell electrochemical properties.

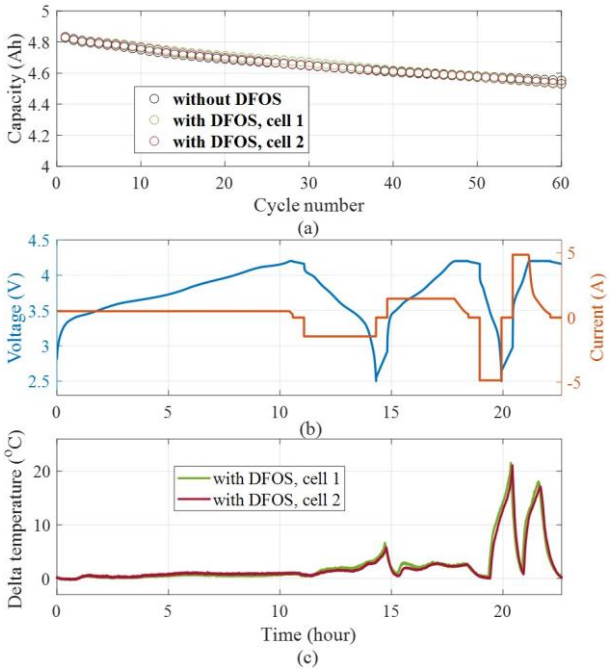

Fig. 2. Comparation of cell performance: (a) capacity retention up to 60 cycles, (b) voltage and current during cycling, and (c) maximum internal temperature change captured by DFOS during cycling.

In particular, Fig. 2 (a) compares the capacity retention up to 60 cycles (under 1 C) of the pristine (without DFOS) and smart cells (with DFOS). Results show that the capacity of the pristine cell after 60 cycles is 4.54 Ahr, while the capacity of the modified smart cells are 4.48 Ahr and 4.49 Ahr, respectively. This indicates that the embedded DFOSs do not negatively impact the cell's electrochemical properties. The current and voltage during cycling for two smart cells are shown in Fig. 2 (b), in response to Fig. 2 (c), where the maximum internal temperature changes collected by the DFOS are plotted. Results suggest that the maximum internal temperature changes of the two smart cells agree closely with each other. This well validates the high reproducibility of the sensor-embedment approach as well as the high reliability of the sensing data.

III. Multi-State Joint Observation

By embedding the micro DFOS, the designed smart battery manifests itself with the internal and surface temperature self-sensing in a real-time, synchronous, and space-resolved fashion. With the newly-obtained sensing data, this section goes further to propose a low-order observer for the joint estimation of heat generation rate, SOC, and maximum capacity of LIB.

A. Thermal Characterization and Parameterization

By assuming a homogeneous temperature distribution along the longitudinal axis, a simplified one-state thermal model of cylindrical battery is given by

$$C_c \frac{dT_c(t)}{dt} = \frac{T_s(t) - T_c(t)}{R_c} + Q(t) \tag{6}$$

where T_c and T_s respectively represent the longitudinal average of core temperature and surface temperature of the battery, C_c and R_c respectively represent the thermal capacity and thermal resistance of the core, while Q denotes the heat generation rate which is calculated by:

$$Q(t) = I_L(t)\left(V_{oc}(z(t)) - V_t(t)\right) - \lambda I_L(t) T_a(t) \tag{7}$$

where I_L is the load current (positive for discharge), V_{oc} the open circuit voltage (OCV), z the SOC, V_t the terminal voltage, T_a the average of core and surface temperature. The first term includes the joule heating and energy associated with the electrode over-potentials which is always positive. The second term is the reversible entropic heat, in which λ is the entropic coefficient.

The parameters in the one-state thermal model that need to be identified include C_c, R_c, and λ. By substituting (7) into (6), the one-state thermal model is expressed as:

$$\begin{aligned} C_c \frac{dT_c(t)}{dt} = \frac{T_s(t) - T_c(t)}{R_c} + I_L(t)\left(V_{oc}(t) - V_t(t)\right) \\ - \lambda I_L(t) T_a(t) \end{aligned} \tag{8}$$

Transforming (8) into the Laplace domain gives

$$sT_c(s) = \frac{T_s(s) - T_c(s)}{R_c C_c} + I_L(s)\frac{V_{oc}(s) - V_t(s) - \lambda T_a(s)}{C_c} \tag{9}$$

where s is the Laplace operator.

The regression model of (9) is given by

$$Z(s) = \boldsymbol{\theta}^{\mathrm{T}} \boldsymbol{\Phi}(s)$$

$$Z(s) = sT(s) \quad \boldsymbol{\theta} = [\alpha \quad \beta \quad \gamma]$$

$$\boldsymbol{\Phi}(s) = \left[T_s(s) - T_c(s) \quad I_L(s)\left(V_{oc}(s) - V_t(s)\right) \quad -I_L(s) T_a(s)\right]^T$$

where $Z(s)$ is the output, $\boldsymbol{\Phi}(s)$ the input, $\boldsymbol{\theta}$ the parametric vector, $\alpha = 1 / R_c C_c$, $\beta = 1/C_c$, $\gamma = \lambda / C_c$. The commonly-used least squares algorithm is employed to identify the parametric vector $\boldsymbol{\theta}$. The estimates of the model parameters can be subsequently obtained by:

$$C_c = \frac{1}{\hat{\beta}},\ R_c = \frac{\hat{\beta}}{\hat{\alpha}},\ \lambda = \frac{\hat{\gamma}}{\hat{\beta}} \tag{10}$$

where the superscript ^ denotes the estimate.

It is worth noting that all the input and output of the regression model are measurable except for the V_{oc}, which is indispensable for the parameter identification. To surmount this problem, the relationship between the SOC and OCV is identified by polynomial fitting the experiment data of SOC-OCV test. The experimental and the fitted SOC-OCV map are plotted in Fig. 3 comparatively. In this way, V_{oc} can be obtained by the corresponding SOC determined by coulomb counting provided a precisely-known initial SOC. Hence, the model parameters are identified offline under 1C constant discharging mode. Specifically, λ is identified at each SOC point in the range from 0% to 100% to build the relationship between λ and SOC, as it is highly dependent on SOC [13].

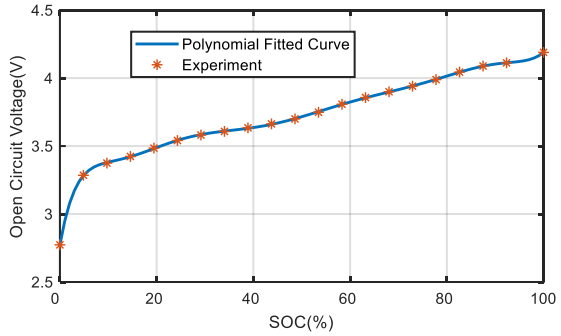

Fig. 3. Polynomial-fitted and experimental data of SOC-OCV correlation.

B. Multi-State Observer

The discrete-time form of the one-state thermal model is given by:

$$C_c\left(T_c(k+1)-T_c(k)\right) = \frac{T_s(k)-T_c(k)}{R_c} + Q(k) \tag{11}$$

As a unique merit of the developed smart battery, T_c is measurable by the embeded DFOS so that the heat generation rate can be calculated straitforwardly by:

$$Q_m(k) = C_c\left(T_c(k+1)-T_c(k)\right) - \frac{T_s(k)-T_c(k)}{R_c} \tag{12}$$

where Q_m denotes the heat generation calculated by core and surface temperature. Hence, by substituting the Q_m into (7), V_{oc} can be calculated directly, and the SOC can be inferred easily from the V_{oc} referring to the calibrated SOC-OCV relationship. However, the V_{oc} estimated via this approach is volunerable to be contaminated by the measurement noises and modeling uncertainties. The perturbations in the V_{oc} estimate can impair the accuracy of SOC estimate, especially for the flat region of the SOC-OCV curve, where a small V_{oc} error will result in a large SOC error. To surmount this problem, an EKF-based state estimator applying Q_m as the noisy system measurement is formulated to estimate the SOC and capacity jointly.

The dynamic equation of the SOC in the discrete-time domain is given by:

$$z(k+1) = z(k) - I_L(k)\Delta t / C_n(k) \tag{13}$$

where C_n denotes the battery capacity with the unit of ampere-seconds, Δt the sampling interval.

By defining the state vector as $\boldsymbol{x} = [z\ 1/C_n]^{\mathrm{T}}$, the noisy measurement as $y = Q_m$, and heat generation model (7) as the observation equation, the discrete-time state-space function can be established as the following general form:

$$\begin{aligned} \boldsymbol{x}(k+1) &= \boldsymbol{A}(k)\boldsymbol{x}(k) + \boldsymbol{w}(k) \\ y(k) &= G\left(\boldsymbol{x}(k)\right) + v(k) \end{aligned} \tag{14}$$

where

$$\begin{aligned} \boldsymbol{A}(k) &= \begin{bmatrix} 1 & -I_L(k)\Delta t \\ 0 & 1 \end{bmatrix} \\ G\left(\boldsymbol{x}(k)\right) &= I_L(k)\left[f\left(z(k)\right) - V_t(k) - \lambda T_a(k) \right] \end{aligned} \tag{15}$$

where $\boldsymbol{w}(k)$ is the process noise, $v(k)$ is the measurement noise which represent the estimation error of the heat generation rate by (12). $\boldsymbol{w}(k)$ and $v(k)$ are assumed to be Gaussian white noise with variances of $\boldsymbol{\delta}_{\mathrm{w}}$ and δ_v, respectively.

Herein, $f(\cdot)$ is the polynomial-fitted SOC-OCV function, which is expressed by:

$$f\left(z(k)\right) = \sum_{i=0}^{n} c_i z^i \tag{16}$$

where n is the maximum fitting order, c_i ($i = 0, 1, \ldots, n$) are the polynomial coefficients. Based on the state-space function (16), the state vector is estimated by EKF algorithm in this paper. Targeting at the specific problem, the algorithmic procedures are summarized in Table I. The relevant matrix $C(k)$ is updated at each iteration as:

$$\hat{\boldsymbol{C}}(k) = \frac{\partial G\left(\boldsymbol{x}(k)\right)}{\partial \boldsymbol{x}(k)}\Big|_{\bar{x}(k)} = \left[I_L(k)\frac{df\left(z(k)\right)}{dz(k)}\Big|_{\bar{z}(k)} \quad 0 \right] \tag{17}$$

Table I. Algorithm procedure of EKF for state joint estimation

Initialize $\hat{\boldsymbol{x}}(0), \hat{P}(0), \boldsymbol{\delta}_w$, and δ_v ; For $k = 1, 2, \ldots$
Priori state update: $\bar{\boldsymbol{x}}(k) = \boldsymbol{A}(k)\hat{\boldsymbol{x}}(k-1)$
Prior error covariance update: $\bar{P}(k) = \boldsymbol{A}(k)\hat{P}(k-1)\boldsymbol{A}^T(k) + \boldsymbol{\delta}_w$
Kalman gain update: $L(k) = \bar{P}(k)\hat{\boldsymbol{C}}(k)^T\left[\hat{\boldsymbol{C}}(k)\bar{P}(k)\hat{\boldsymbol{C}}(k)^T + \delta_v\right]^{-1}$
Posterior state update: $\hat{\boldsymbol{x}}(k) = \hat{\boldsymbol{x}}(k-1) + L(k)\left[Q_m(k) - G\left(\bar{\boldsymbol{x}}(k)\right)\right]$
Posterior error covariance update: $\hat{P}(k) = \left(I - L(k)\hat{\boldsymbol{C}}(k)\right)\bar{P}(k)$

C. Overall Algorithmic Framework

The overall algorithmic framework is illustrated in Fig. 4. Leveraging the measured voltage, current, surface and internal temperature, the parameters of the one-state thermal model is determined via the principle of temperature mismatch minimization. Depending on the parameterized thermal model, the heat generation rate, SOC, and maximum capacity can be estimated jointly by simple mathematical manipulations described in (12) and a low-order EKF-based observer.

Remark: The state joint estimation with electrical model is a vast area of intensive studies, while the thermal model-based estimation has never been explored before, possibly due to the

barrier of measuring the battery internal temperature. Compared to the conventional electrical model-based method, the proposed method promises a two-fold benefit:

(1) The parameterization of the one-state thermal model is much easier than that of the electrical model. Due to the high sensitivity to SOC, health state and temperature, parameters of the electrical model need to be identified online to maintain a high modeling accuracy [38-40]. In contrast, the thermal parameters are affected by the material properties and the craft of electrode assembly and casing, which are relatively stable. Hence, the one-state thermal model only needs to be offline parameterized once or periodically in practice.

(2) The heat generation rate can be also calculated directly by the proposed method. The internal distributive temperature sensing and heat generation rate estimation open new paradigm for the diagnosis and pre-warning of the catastrophic internal short circuit and thermal runaway.

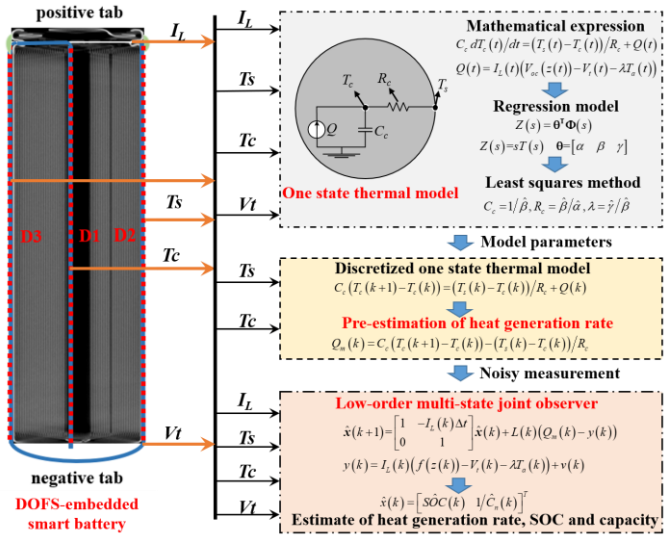

Fig. 4. Overall algorithmic framework of the proposed method.

IV. Results and Discussion

A. Distributed Temperature Sensing

After demonstrating the repeatability of the measurements and that the cells are fundamentally unchanged, the cells were cycled using 0.3 C and 1 C for CC discharge and CC-CV charge with a 30 minutes rest interval to represent standard cycling for the 21700 cylindrical cells. The temperature measurement results during the cycling tests are shown in Fig. 5.The internal temperature distribution D1, external temperature distribution near the positive tab D2, and that near the negative tab D3 are illustrated in Fig. 5 (b), (c), and (d), respectively. The schematic of the smart battery with dimension and direction is illustrated in Fig. 5 (e), where the full measurement length of the DFOS for D1, D2 and D3 are 6.7 cm in the direction from the negative terminal to the positive terminal. A spatial measurement resolution of 2.6 mm is achieved along the *y*-axis (fiber length) in Fig. 5 (b, c and d).

It is observed from Fig. 5 (b-d) that the temperature for D1, D2 and D3 are not uniformly distributed. The measured temperature of D2 indicates that the surface area near the positive tab was hotter as it gets closer to the positive terminal. This is due to the heat generated by the positive tab during discharge. Conversely, the surface area near the negative tab (D3) shows a higher temperature in the bottom area of the cylindrical cell due to the half-length of the negative tab from the bottom of the can. The measured internal temperature is found to be higher than the external temperature. Moreover, it is found that the temperature difference (between internal and external temperature along the perpendicular radial axis) is location dependent due to the asymmetrical structure of cylindrical cell.

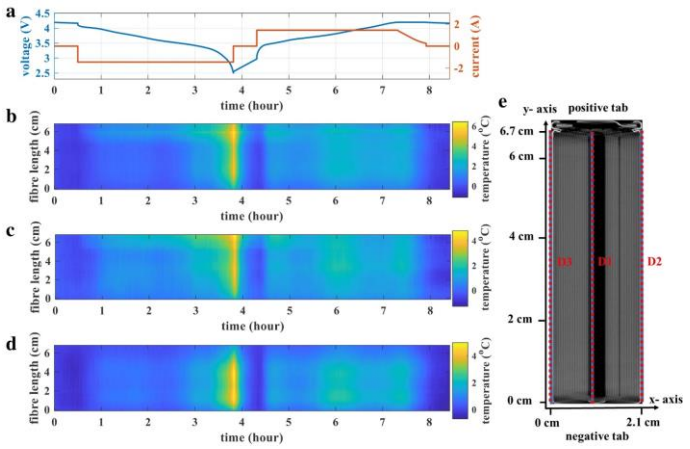

Fig. 5. Temperature measurement at 0.3 C cycling: (a) current/voltage, (b) core temperature distribution (D1), external temperature distribution along (c) D2, (d) D3, and (e) schematic of the smart battery.

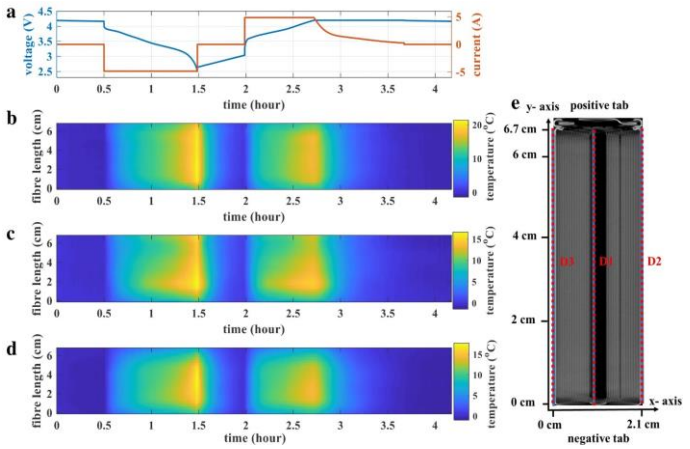

Fig. 6. Temperature measurement at 1 C cycling: (a) current/voltage, (b) core temperature distribution (D1), external temperature distribution along (c) D2, (d) D3, and (e) schematic of the smart battery.

Fig. 6 shows the evolution of the internal (D1) and surface (D2 and D3) temperature distribution synchronized with current and voltage (Fig. 6 (a)) during 1 C discharge and 1 C CC-CV charge. As observed in Fig. 6 (b), the internal temperature shows a more uniform format compared with the scenario of 0.3 C cycling. During this test, the middle of the cell is obviously hotter than the positive and negative terminals, due to the substantial heat accumulation and slow dissipation under

high-rate conditions. The internal temperature exhibits a more uniform distribution compared with the surface measurements (D2 and D3). Comparing Fig. 5 (c) with Fig. 6 (c), another temperature peak occurs under the high C-rate, which are positioned approximately 2 cm from the negative terminal. This is in addition to the temperature peak close to the positive tab at low C-rate. With respect to the surface temperature (D3) distribution at 1 C, it shows a similar profile compared to that at 0.3 C, where the local high temperature is around the center of cell near the negative terminal. However, the temperature gradient is much more pronounced in this case. These observations further reinforce the conclusion that the temperature gradient between cell core and surface is location dependent along the length of the cell's aluminum can.

B. Validation of Thermal Modeling

The fidelity of thermal modeling is essential to the model-based state joint observation method. The results of cycling experiments are hence employed to validate the developed one-state thermal model herein.

The modeled battery core temperatures are plotted against their embedded DFOS-based measurements in Fig. 7 under different cycling C-rates. It is shown that the modeled core temperatures resemble the benchmarks closely for the entire experiment in both cases. The build-up of core temperature is observably more obvious under the 1 C-discharge scenario, contributed by the elevated heat generation. Interestingly, the core temperature of LIB does not build up monotonously for the 0.3 C-discharge case, witnessed by the temperature shrink at the middle SOC range. This can be attributed to the slight heat generation rate at low-rate condition as opposed to the intensity of heat transfer and convection. This however does not skew the modeling results. As shown in Fig. 7 (c) and (d), the modeling errors under 0.3 C and 1 C discharging cases are both well confined within the ± 0.1 ℃ error bound. In particular, the rooted mean squared error (RMSE) of temperature modeling for the two scenarios are as low as 0.0475 ℃ and 0.0305 ℃, respectively. The results suggest that the embedded DFOS-enabled parameterization and the resultant thermal model are highly authentic to simulate the practical thermal responses.

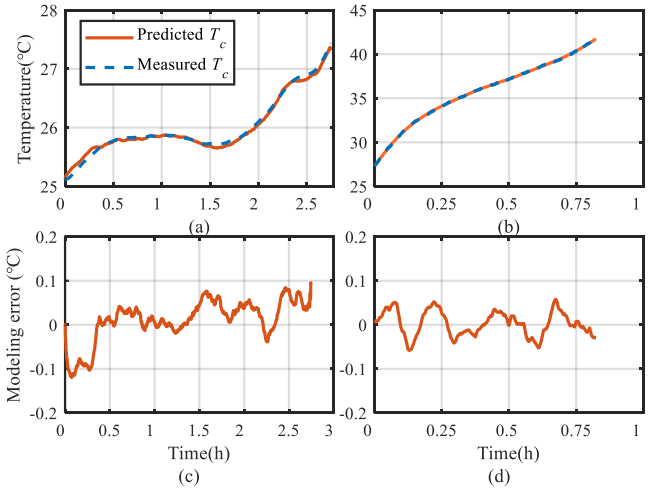

Fig. 7. Modeled and benchmarked core temperature under (a) 0.3 C and (b) 1 C CC discharging, and (c-d) the corresponding modeling error.

C. Validation of Heat Generation Rate Estimation

The ground truth of heat generation rate should be known to evaluate the estimation performance. Herein, the reference heat generation rate is determined by (7), where V_{oc} is inferred from the SOC-OCV function with the pre-calibrated SOC. It is worth noting that this reference value cannot be obtained in practical applications due to the lack of calibrating environment. The heat generation rates estimated by the proposed method and the commonly-used electrical model-based method are plotted against the benchmarks in Fig. 8. The statistical comparisons are shown in Table. II. In the electrical model-based method, the estimated SOC is used to calculate the heat generation via (7). It is observed in Fig. 8 (a, b) that the heat generation rates estimated by the proposed method are in close agreement with the reference trajectory, justifying the high estimation accuracy. Affected by the measurement noises, the estimates are contaminated by non-ignorable stochastic errors, which are visually severer under 0.3 C condition considering the much smaller heat generation rates. This testifies about the necessity of EKF-based observation, i.e., the pre-estimation error of Q_m, if directly reversed to the V_{oc} estimate, can be transferred and hence impair the entire close loop of multi-state estimation. However, as shown in Fig. 8 (c, d) and Table. II, the stochastic errors in the two cases exhibit similar and acceptable amplitude, which is well confined within the 0.1 W error bound. By comparison, the electrical model-based estimates deviate from the ground truth with larger errors due to the limited accuracy of SOC estimation, which will be elaborated in the next section. The comparative results suggest that the embedded DFOS-enabled heat generation rate estimation has high precision and favorable online tractability, considering the slight computing effort with several simple mathematical manipulations.

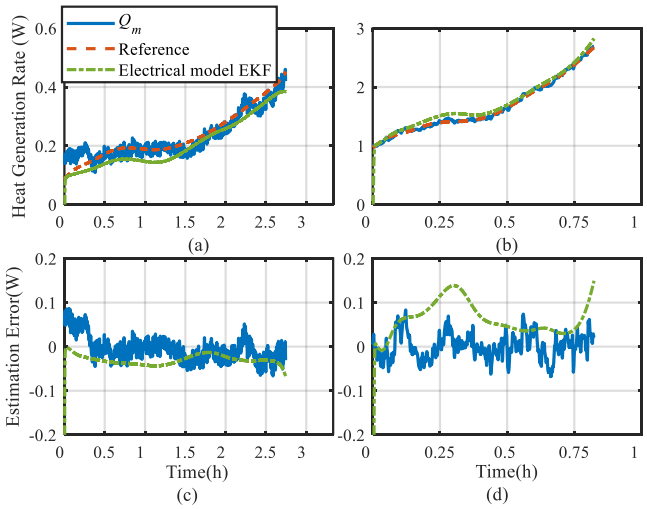

Fig. 8. Estimated and reference heat generation rate under (a) 0.3 C and (b) 1 C discharging, and (c-d) the corresponding estimation error.

Table. II MAE and RMSE of heat generation rate estimation

	Proposed method	Electrical model-based method

	0.3 C	1 C	0.3 C	1 C
MAE	0.023 W	0.024 W	0.030 W	0.038 W
RMSE	0.030 W	0.035 W	0.034 W	0.069 W

D. Validation of SOC and Capacity Estimation

This section goes further to validate the effectiveness of the proposed method for SOC and maximum capacity estimation. The states are initialized substantially away from the true values for both methods as they are not known in practical scenarios. CC-CV charging is applied to fully charge the cell, and then CC discharge is applied to preset the cell at a known SOC. Being aware of the initial SOC, the benchmarked SOC during the subsequent experiment can be obtained leveraging the coulomb counting method. It is worth noting that all the parameters of the electrical model and the thermal model are identified offline.

The estimation results under both 0.3 C and 1 C discharging conditions are plotted comparatively in Fig. 9, while the estimation errors after convergence are tabulated in Table. III. It is observed that the proposed method converges slower than the electrical model-based one, due to the low accuracy of heat generation estimation at the initial stage, as shown in Fig. 8. However, the estimation accuracy of the proposed method is obviously higher than that of the electrical model-based EKF. This is because the offline identified electrical model cannot guarantee the accuracy under different working conditions. The electrical parameters are dependent on many factors such as the charge/discharge rate, temperature and SOC. In contrast, the thermal parameters of the battery are much more stable during normal operations, and thereby the offline-identified thermal model can promise a more accurate estimation.

Another finding is that the estimation accuracy at 0.3 C is lower than that at 1C for the proposed method. This can be explained by the observations in Fig. 8, where the signal-noise ratio of the heat generation rate estimation is much lower under 0.3 C condition. Since the heat generation rate serves as the system output of state-space model, the heavier disturbance on it deteriorates the SOC estimation inevitably. This fact also indicates that the proposed observation method is theoretically more accurate in high-rate applications. In spite of this, the accuracy of the proposed method in 0.3 C discharging mode is still higher than the electrical model-based EKF.

The estimation results of battery maximum capacity are plotted comparatively in Fig. 9 (e) and (f). As observed, it takes some time for the two methods to converge to the ground truth from the initial offset. However, this is not a critical problem as the maximum capacity is slow varying and only diagnosed in a long timescale in practical applications. The maximum capacity estimated by the electrical model-based method deviates substantially from the reference value in the SOC range of 40% ~ 15%, which is consistent with the large deviation of SOC estimation within this region. By comparison, the proposed method gives rise to a visibly much more stable and accurate estimation, which coincides with the improved SOC estimation accuracy. Quantitatively, the MAE of maximum capacity estimation is only 0.12 Ahr by using the proposed method. It is also observed that the capacity estimation error at 1 C is lower than that at 0.3 C. This is within expectation as the estimation of maximum capacity and SOC are cross-linked intrinsically and closely.

The observed encouraging results suggest that associated with the DFOS-based temperature matrix sensing, the proposed method can realize the high-fidelity joint estimation of the heat generation rate, SOC, and maximum capacity in a real-time fashion. The accuracy improvement opposed to the commonly-used electrical model-based method is prominent, attributed to the better stability of thermal parameters once determined. Last but essentially, the proposed method appeals more to the high-rate application scenarios where the heat generation rate plays a more pronounced role.

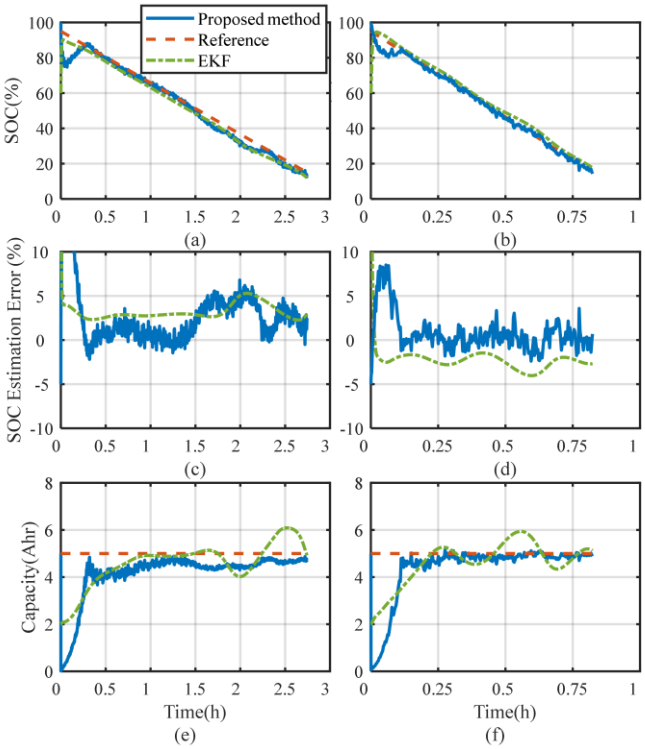

Fig. 9. Results of SOC and capacity estimation: SOC estimation under (a, c) 0.3 C and (b, d) 1 C discharging mode, capacity estimation under (e) 0.3 C and (f) 1 C discharging mode.

Table. III MAE and RMSE of SOC estimation

	Proposed method		Electrical model-based method	
	0.3 C	1 C	0.3 C	1 C
MAE	2.07%	0.79%	3.17%	2.43%
RMSE	2.65%	1.02%	3.27%	2.52%

E. Robustness to Battery Aging

Both the electrical and thermal parameters are subjected to variations accompanied with the aging of LIB. Therefore, it is highly practical to evaluate the robustness of methods against the battery aging. The estimation results of SOC and maximum capacity are plotted comparatively in Fig. 10. The errors of SOC estimation are tabulated in Table. IV correspondingly. It can be seen in Fig. 10 (a-d) that the performance of electrical model-based method is deteriorated remarkably after aging occurs. Comparing Table. III and Table. IV reveals the same conclusion, especially for the 1C discharging condition. The

capacity estimation also exhibits large fluctuations at low-SOC regions. These observations can be explained by the large biases of impedance parameters, which affect heavily the model-based estimation framework.

Instead, it is observed that the proposed method is much less affected by the aging of battery. The error of SOC estimation builds up mildly after aging, especially for the 1C condition. The capacity estimation is also maintained at a similar accuracy compared to the cases before aging. This is supposed to be attributed to the relatively stable thermal properties of batteries within certain aging statuses. The comparative results suggest that the proposed method outperforms the electrical model-based benchmark in terms of the robustness to the aging. To ensure a reasonable accuracy, the commonly-used electrical model-based observer needs more frequent re-calibration, while the proposed method promises high-fidelity estimation within a long aging scope.

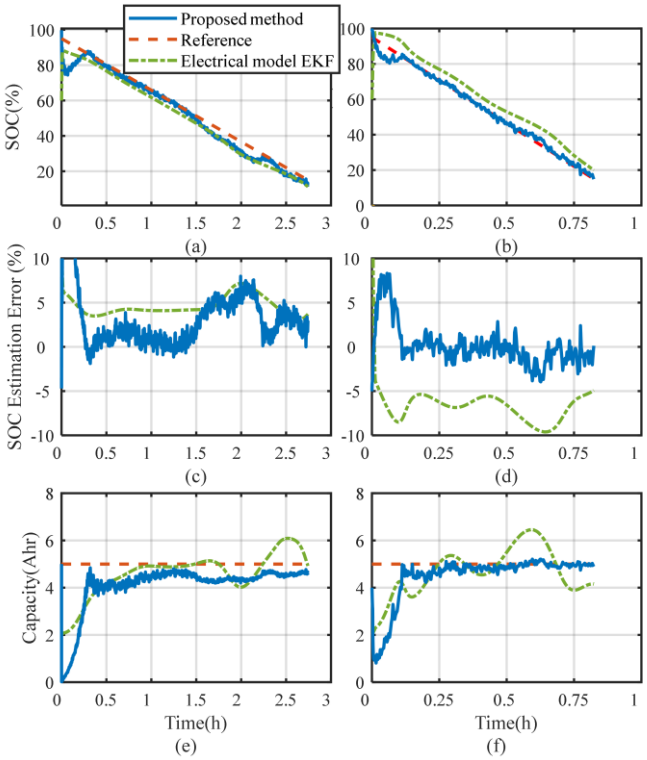

Fig. 10. Results of SOC and capacity estimation with an aged battery: SOC estimation under (a, c) 0.3 C and (b, d) 1 C discharging mode, capacity estimation under (e) 0.3 C and (f) 1 C discharging mode.

Table. IV MAE and RMSE of SOC estimation with an aged battery

	Proposed method		Electrical model-based method	
	0.3 C	1 C	0.3 C	1 C
MAE	3.12%	1.39%	4.58%	6.9%
RMSE	4.43%	2.15%	4.71%	7%

V. Conclusions and Future Work

A novel smart battery structure with embedded DFOS is proposed in this paper for space-resolved temperature matrix sensing. Supported by the new sensing data, a thermal model-based approach is further proposed for the low-order multi-state joint observation of the smart battery. Experiments have been performed to validate the proposed configuration and observer. The primary conclusions are summarized as follows:

(1) The temperature gradient between the core and surface of cylindrical cell is location dependent along the length of aluminum can. The configured smart cell embedding DFOS can realize a real-time distributed sensing of the temperature matrix with a high space resolution of 2.6 mm, thus presents much scope for the temperature inhomogeneity detection of LIB.

(2) Enabled by the embedded DFOS, the thermal parameters of LIB can be identified easily, and the resultant thermal model are highly accurate to simulate the battery thermal responses, with the errors confined to ± 0.1 ℃ error bound.

(3) With the thermal model-based multi-state observer, the heat generation rate, SOC, and maximum capacity are online estimated precisely, where the MAEs of estimation are 0.035 W, 0.79% and 0.12 Ahr, respectively. The proposed method validates to outperform the commonly-used electrical model-based method substantially regarding the estimation accuracy and the robustness to battery aging.

Only the means of surface/core temperature are utilized for the multi-state estimation in this work. Improvement towards distributed thermal modeling and the associated observer design can be an important topic for future work, in which the distributed temperature measurements are indispensable for the parameter identification and model validation. Moreover, the distributed temperature measurements have great potential to be deployed in battery thermal fault diagnosis, especially for the localization of battery thermal fault. This endeavor will be focused in our future work.

References

[1] X. Tang, F. Gao, K. Liu, Q. Liu, and A. M. Foley, "A Balancing Current Ratio based State-of-Health Estimation Solution for Lithium-ion Battery Pack," *IEEE Transactions on Industrial Electronics*, pp. 1-1, 2021.

[2] Q. Ouyang, J. Chen, and J. Zheng, "State-of-Charge Observer Design for Batteries With Online Model Parameter Identification: A Robust Approach," *IEEE Transactions on Power Electronics*, vol. 35, pp. 5820-5831, 2020.

[3] A. Samanta and S. S. Williamson, "A Survey of Wireless Battery Management System: Topology, Emerging Trends, and Challenges," *Electronics*, vol. 10, p. 2193, 2021.

[4] A. Samanta and S. S. Williamson, "A comprehensive review of lithium-ion cell temperature estimation techniques applicable to health-conscious fast charging and smart battery management systems," *Energies*, vol. 14, p. 5960, 2021.

[5] M. Farag, H. Sweity, M. Fleckenstein, and S. Habibi, "Combined electrochemical, heat generation, and thermal model for large prismatic lithium-ion batteries in real-time applications," *Journal of Power Sources*, vol. 360, pp. 618-633, 2017.

[6] Y. Yin, Z. Zheng, and S.-Y. Choe, "Design of a calorimeter for measurement of heat generation rate of lithium ion battery using thermoelectric device," *SAE International Journal of Alternative Powertrains*, vol. 6, 2017.

[7] M. Song, Y. Hu, S.-Y. Choe, and T. R. Garrick, "Analysis of the Heat Generation Rate of Lithium-Ion Battery Using an Electrochemical Thermal Model," *Journal of The Electrochemical Society*, vol. 167, p. 120503, 2020/08/06 2020.

[8] X. Feng, X. He, L. Lu, and M. Ouyang, "Analysis on the Fault Features for Internal Short Circuit Detection Using an

Electrochemical-Thermal Coupled Model," *Journal of The Electrochemical Society*, vol. 165, pp. A155-A167, 2018.
[9] H. Dai, L. Zhu, J. Zhu, X. Wei, and Z. Sun, "Adaptive Kalman filtering based internal temperature estimation with an equivalent electrical network thermal model for hard-cased batteries," *Journal of Power Sources*, vol. 293, pp. 351-365, 2015.
[10] Y. Xie, W. Li, X. Hu, C. Zou, F. Feng, and X. Tang, "Novel mesoscale electrothermal modeling for lithium-ion batteries," *IEEE Transactions on Power Electronics*, vol. 35, pp. 2595-2614, 2019.
[11] G. Liu, M. Ouyang, L. Lu, J. Li, and X. Han, "Analysis of the heat generation of lithium-ion battery during charging and discharging considering different influencing factors," *Journal of Thermal Analysis and Calorimetry*, vol. 116, pp. 1001-1010, 2014/05/01 2014.
[12] J. Zhang, X.-G. Yang, F. Sun, Z. Wang, and C.-Y. Wang, "An online heat generation estimation method for lithium-ion batteries using dual-temperature measurements," *Applied Energy*, vol. 272, p. 115262, 2020.
[13] Y. Hu, S.-Y. Choe, and T. R. Garrick, "Hybridized time-frequency method for the measurement of entropy coefficient of lithium-ion battery," *Electrochimica Acta*, vol. 362, p. 137124, 2020/12/01/ 2020.
[14] S. Dey, H. E. Perez, and S. J. Moura, "Model-Based Battery Thermal Fault Diagnostics: Algorithms, Analysis, and Experiments," *IEEE Transactions on Control Systems Technology*, vol. 27, pp. 576-587, 2019.
[15] M. Parhizi, M. Ahmed, and A. Jain, "Determination of the core temperature of a Li-ion cell during thermal runaway," *Journal of Power Sources*, vol. 370, pp. 27-35, 2017.
[16] C. Zou, X. Hu, Z. Wei, T. Wik, and B. Egardt, "Electrochemical estimation and control for lithium-ion battery health-aware fast charging," *IEEE Transactions on Industrial Electronics*, vol. 65, pp. 6635-6645, 2018.
[17] K. Liu, K. Li, and C. Zhang, "Constrained generalized predictive control of battery charging process based on a coupled thermoelectric model," *Journal of Power Sources*, vol. 347, pp. 145-158, 2017.
[18] D. Zhang, S. Dey, H. E. Perez, and S. J. Moura, "Real-time capacity estimation of lithium-ion batteries utilizing thermal dynamics," *IEEE Transactions on Control Systems Technology*, vol. 28, pp. 992-1000, 2019.
[19] Y. Li, B. Xiong, M. Vilathgamuwa, Z. Wei, C. Xie, and C. Zou, "Constrained Ensemble Kalman Filter for Distributed Electrochemical State Estimation of Lithium-Ion Batteries," *IEEE Transactions on Industrial Informatics*, 2020.
[20] Y. Li, Z. Wei, B. Xiong, and D. M. Vilathgamuwa, "Adaptive Ensemble-Based Electrochemical-Thermal-Degradation State Estimation of Lithium-Ion Batteries," *IEEE Transactions on Industrial Electronics*, 2021.
[21] X. Lin, H. E. Perez, J. B. Siegel, and A. G. Stefanopoulou, "Robust estimation of battery system temperature distribution under sparse sensing and uncertainty," *IEEE Transactions on Control Systems Technology*, vol. 28, pp. 753-765, 2019.
[22] C. Zou, X. Hu, Z. Wei, and X. Tang, "Electrothermal dynamics-conscious lithium-ion battery cell-level charging management via state-monitored predictive control," *Energy*, vol. 141, pp. 250-259, 2017.
[23] J. Zhu, Z. Sun, X. Wei, and H. Dai, "A new lithium-ion battery internal temperature on-line estimate method based on electrochemical impedance spectroscopy measurement," *Journal of Power Sources*, vol. 274, pp. 990-1004, 2015.
[24] R. R. Richardson and D. A. Howey, "Sensorless battery internal temperature estimation using a Kalman filter with impedance measurement," *IEEE Transactions on Sustainable Energy*, vol. 6, pp. 1190-1199, 2015.
[25] R. R. Richardson, P. T. Ireland, and D. A. Howey, "Battery internal temperature estimation by combined impedance and surface temperature measurement," *Journal of Power Sources*, vol. 265, pp. 254-261, 2014.
[26] A. Reinfelder, N. Martiny, and A. Jossen, "Thermal in-cell measurement for li-ion pouch cells," in *Conference in Future Automotive Technology*, 2012.
[27] N. Martiny, A. Rheinfeld, J. Geder, Y. Wang, W. Kraus, and A. Jossen, "Development of an all kapton-based thin-film thermocouple matrix for in situ temperature measurement in a lithium ion pouch cell," *IEEE Sensors Journal*, vol. 14, pp. 3377-3384, 2014.
[28] S. Zhu, J. Han, H.-Y. An, T.-S. Pan, Y.-M. Wei, W.-L. Song, *et al.*, "A novel embedded method for in-situ measuring internal multi-point temperatures of lithium ion batteries," *Journal of Power Sources*, vol. 456, p. 227981, 2020.
[29] C.-Y. Wang, G. Zhang, S. Ge, T. Xu, Y. Ji, X.-G. Yang, *et al.*, "Lithium-ion battery structure that self-heats at low temperatures," *Nature*, vol. 529, pp. 515-518, 2016.
[30] Z. Wei, J. Zhao, H. He, G. Ding, H. Cui, and L. Liu, "Future smart battery and management: Advanced sensing from external to embedded multi-dimensional measurement," *Journal of Power Sources*, vol. 489, p. 229462, 2021.
[31] A. Fortier, M. Tsao, N. D. Williard, Y. J. Xing, and M. G. Pecht, "Preliminary Study on Integration of Fiber Optic Bragg Grating Sensors in Li-Ion Batteries and In Situ Strain and Temperature Monitoring of Battery Cells," *Energies*, vol. 10, Jul 2017.
[32] S. Novais, M. Nascimento, L. Grande, M. F. Domingues, P. Antunes, N. Alberto, *et al.*, "Internal and External Temperature Monitoring of a Li-Ion Battery with Fiber Bragg Grating Sensors," *Sensors (Basel)*, vol. 16, Aug 30 2016.
[33] T. Amietszajew, E. McTurk, J. Fleming, and R. Bhagat, "Understanding the limits of rapid charging using instrumented commercial 18650 high-energy Li-ion cells," *Electrochimica Acta*, vol. 263, pp. 346-352, Feb 10 2018.
[34] J. Fleming, T. Amietszajew, E. McTurk, D. P. Towers, D. Greenwood, and R. Bhagat, "Development and evaluation of in-situ instrumentation for cylindrical Li-ion cells using fibre optic sensors," *HardwareX*, vol. 3, pp. 100-109, 2018.
[35] E. McTurk, T. Amietszajew, J. Fleming, and R. Bhagat, "Thermo-electrochemical instrumentation of cylindrical Li-ion cells," *Journal of Power Sources*, vol. 379, pp. 309-316, Mar 2018.
[36] J. Huang, L. Albero Blanquer, J. Bonefacino, E. R. Logan, D. Alves Dalla Corte, C. Delacourt, *et al.*, "Operando decoding of chemical and thermal events in commercial Na(Li)-ion cells via optical sensors," *Nature Energy*, 2020.
[37] J. Peng, Y. Jin, S. Jia, and S. Xu, "External Electrode Temperature Monitoring of Lithium Iron Phosphate Batteries Based on Fiber Bragg Grating Sensors," *IOP Conference Series: Earth and Environmental Science*, vol. 495, 2020.
[38] J. Meng, D. Stroe, M. Ricco, G. Luo, and R. Teodorescu, "A Simplified Model-Based State-of-Charge Estimation Approach for Lithium-Ion Battery With Dynamic Linear Model," *IEEE Transactions on Industrial Electronics*, vol. 66, pp. 7717-7727, 2019.
[39] A. Chen, W. Zhang, C. Zhang, W. Huang, and S. Liu, "A Temperature and Current Rate Adaptive Model for High-Power Lithium-Titanate Batteries Used in Electric Vehicles," *IEEE Transactions on Industrial Electronics*, vol. 67, pp. 9492-9502, 2020.
[40] X. Du, J. Meng, Y. Zhang, X. Huang, S. Wang, P. Liu, *et al.*, "An Information Appraisal Procedure Endows Reliable Online Parameter Identification to Lithium-ion Battery Model," *IEEE Transactions on Industrial Electronics*, pp. 1-1, 2021.

Zhongbao Wei (M'19–SM'21) received the B.Eng. and the M.Sc. degrees in instrumental science and technology from Beihang University, China, in 2010 and 2013, and the Ph.D. degree in power engineering from Nanyang Technological University, Singapore, in 2017.

He has been a research fellow with Energy Research Institute @ NTU, Nanyang Technological University from 2016 to 2018. He is currently a professor in vehicle engineering with the National Engineering Laboratory for Electric Vehicles, Beijing Institute of Technology, China. He has authored more than 80 peer-reviewed articles. His research interests include electrified transportation and battery management. He serves as Associate Editor for many international journals like IEEE Transactions on Industrial

Electronics, IEEE Transactions on Intelligent Transportation Systems, and IET Intelligent Transport Systems.

Jian Hu received the B.Eng. degree in automotive engineering from the Beijing Institute of Technology, Beijing, China, in 2019. He is currently pursuing the Ph.D. degree in mechanical engineering at Beijing Institute of Technology, Beijing, China.

His research interests include the state estimation, fault diagnosis and modeling of lithium-ion battery system.

Hongwen He (M'03–SM'12) received the M.Sc.degree from Jilin University of Technology, Changchun, China and the Ph.D. degree from Beijing Institute of Technology, Beijing, China, in 2000 and 2003, respectively, both in vehicle engineering. He is currently a Professor with the National Engineering Laboratory for Electric Vehicles, School of Mechanical Engineering, Beijing Institute of Technology. Focusing on the research field of "New Energy Vehicle Drive and Control", he has presided over 18 national-level projects/tasks such as the National Key Research and Development Plan for New Energy Vehicles, the National Natural Science Foundation of China (NSFC) etc. He has published 126 EI-indexed papers, 82 SCI-indexed papers, and 17 ESI highly cited papers. He has been awarded the second prize of the Chinese National Science and Technology Award, the first prize of natural science by the Ministry of Education, the first prize of technological invention of China's automobile industry and the second prize of national defense technology. He received the Best Paper Awards from the journal Energies and the 2017 International Symposium on Electric Vehicles. He is serving in the Editorial Board of Energies and Vehicles. He was the Chair of the 2017 International Conference on Energy, Ecology and Environment held in Stockholm, Sweden.